Comparison between discrete dipole approximation and other modelling methods for the plasmonic response of gold nanospheres

**V. L. Y. Loke · G. M. Huda · E. U. Donev ·
V. Schmidt · J. T. Hastings · M. Pinar Mengüç ·
T. Wriedt**

Abstract We investigate the plasmonic response of gold nanospheres calculated using discrete dipole approximation validated against the results from other discretization methods, namely the finite-difference time-domain method and the finite-element methods. Comparisons are also made with calculations from analytical methods such as the Mie solution and the null-field method with discrete sources. We consider the nanoparticle interacting with the incident field both in free space and sitting on a planar substrate. In the latter case, discrete dipole approximation with surface interaction is used; this includes the interaction with the 'image dipoles' using Sommerfeld integration.

1 Introduction

Noble metals are particularly good electrical conductors due to the number of free electrons that form a negatively
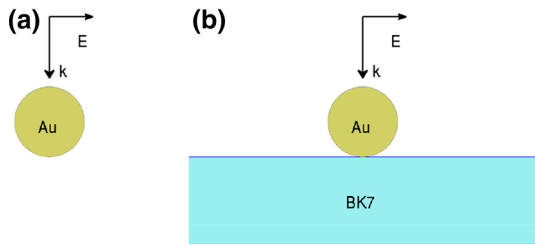
V. L. Y. Loke · V. Schmidt
Mechanische Verfahrenstechnik, University of Bremen,
Bremen, Germany

V. L. Y. Loke (✉)
School of Mathematics and Physics, The University
of Queensland, Queensland, Australia
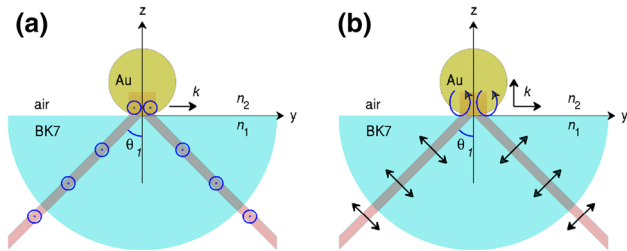e-mail: loke@physics.uq.edu.au

G. M. Huda · E. U. Donev · J. T. Hastings
Department of Electrical and Computer Engineering,
University of Kentucky, Lexington, KY, USA

M. P. Mengüç
School of Engineering, Özyeğin University, Çekmeköy,
Istanbul, Turkey

T. Wriedt
Institut für Werkstofftechnik, University of Bremen,
Bremen, Germany

charged 'cloud' in the lattice of positively charged atomic nuclei. These electrons collectively oscillate when stimulated by an external electric field. When the natural oscillation frequency of the system matches that of the incident field, the *plasmon resonance* [1] phenomenon can be observed. The resonance can occur either with the bulk of the metallic body or confined to its surface. In recent times, the surface plasmon resonance phenomenon of noble metal nanoparticle has found its way into many applications ranging from high-resolution imaging [2], biomarkers for the diagnosis of Alzheimer's [3], targeting cancer cells [4] and lab-on-a-chip immunosensors [5], to name but a few.

Most applications involve clusters or array of nanoparticles, and the morphology of the individual particle is polyhedral [6, 7]. The aim of this paper is to benchmark the discrete dipole approximation with surface interaction (DDA-SI) [8] against other modelling methods when applied to noble metal nanoparticle plasmonics. Although the discretization methods such as DDA [9, 10], finite-element method (FEM) [11] and finite-difference time-domain method (FDTD) [12] can accommodate multiple arbitrary-shaped, inhomogeneous and anisotropic particles, we model a single spherical nanoparticle for ease of standardization, particularly when comparing against the analytical methods. The analytical methods with which we compare are the Lorenz–Mie theory [13, 14] and the null-field method with discrete sources (NFM-DS) [15], a variant of the T-matrix method [16]. A general review of the above-mentioned methods is provided by Wriedt [17].

In the models, the nanoparticle is initially illuminated by a plane wave in free space (Fig. 1a). Next, a substrate is included with the plane wave propagating at normal to the planar surface (Fig. 1b). Finally, an evanescent wave resulting from the total internal reflection (TIR) of a plane

(a)   **(b)**

Fig. 1 Schematic representing the plane illumination of a gold nanoparticle **a** in free space **b** on a BK7 glass substrate

(a)   **(b)**

Fig. 2 Schematic representing the evanescent **a** TE and **b** TM illumination of a gold nanoparticle on a BK7 glass prism (substrate)

wave below the planar surface (Fig. 2) is used as the source of illumination.

2 Modelling methods

We will briefly describe the modelling methods and the respective packages used for comparison. A general comparison including comparative calculation times between DDA, FEM, FDTD, Lorenz–Mie theory and the T-matrix method was presented by Parson et al. [18]. Here, we specifically target the Au sphere, where it is widely known that there is a characteristic peak in its extinction spectrum when its diameter is 50 nm and the incident wavelength is 515–540 nm [19–21], depending on whether it is in air, colloidal or on a substrate. We also

made calculations for the Au sphere with the diameter of 200 nm for comparison.

The dispersion of the refractive indices of the materials used in the models is calculated using continuous functions instead of measured data; for Au, the Drude-critical points [22] formula is used, and for BK7 borosilicate glass, the Sellmeier equation [23] is used (Fig. 3). The reason behind using the analytical function for the dispersion is to address the fundamental incompatibility between the frequency domain measured dispersion data and the FDTD method which is a time-domain method [24].

2.1 DDA and DDA-SI

The DDA approach essentially treats the arbitrarily shaped scatterer(s) as being made up of Rayleigh scatterers, i.e., polarizable dipoles stacked in, usually, the cubic lattice formation. The dipoles react not only to the excitation from the incident field but also to the re-radiation from the other dipoles. DDA assumes the steady state and calculation are performed for one wavelength at a time.

A simple linear system of equations represents the relationship between the incident field, mutual interaction between N dipoles in the scattering structure(s) and the dipole moments [9, 10],

$$\sum_{k=1}^{N} \mathbf{A}_{jk}\mathbf{P}_j = \mathbf{E}_{inc,j}, \tag{1}$$

where $\mathbf{E}_{inc,j}$ is the incident field and $\mathbf{P}_j$ is the unknown dipole moment at dipole j. For DDA, $\mathbf{A}_{jk}$ [25] is the Green tensor $\mathbf{G}_{jk}$,

$$\mathbf{G}_{jk} = \exp(ikr_{jk})\left[\frac{k^2(\hat{r}_{jk}\hat{r}_{jk} - \mathbf{1}_3)}{r_{jk}} + \frac{ikr_{jk} - 1}{r_{jk}^3}(3\hat{r}_{jk}\hat{r}_{jk} - I_3)\right], \tag{2}$$

whereas for DDA-SI, $\mathbf{A}_{jk} = \mathbf{G}_{jk} + \mathbf{R}_{jk}$, where $\mathbf{R}_{jk}$ is the surface interaction term described in [26]. The system of

Fig. 3 Refractive index dispersions of **a** Au calculated using the Drude-critical points model and of **b** BK7 glass calculated using the Sellmeier equation
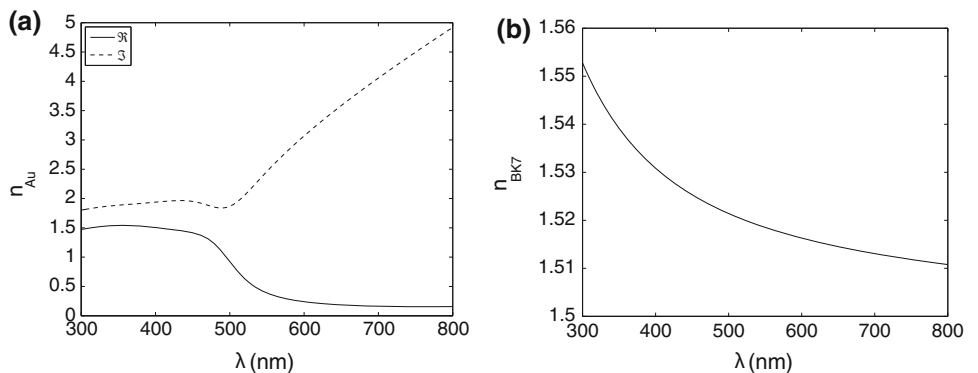
linear equations is usually solved using an iterative method; for this paper, the generalized minimum residual method (gmres) [27] was used.

Having obtained the solution for dipole moments $\mathbf{P}_j$, the extinction and absorption cross sections can be calculated as [10],

$$C_{\text{ext}} = \frac{4\pi k}{|\mathbf{E}_0|^2} \sum_{j=1}^{N} \text{Im}\left(\mathbf{E}_{\text{inc},j}^* \cdot \mathbf{P}_j\right), \tag{3}$$

and

$$C_{\text{abs}} = \frac{4\pi k}{|\mathbf{E}_0|^2} \sum_{j=1}^{N} \left\{ \text{Im}\left[\mathbf{P}_j \cdot (\alpha_j^{-1})^* \mathbf{P}_j^*\right] - \frac{2}{3} k^3 |\mathbf{P}_j|^2 \right\}, \tag{4}$$

respectively, normalized against the intensity of the incident field $|\mathbf{E}_0|^2$, where α_j is the dipole polarizability, calculated using the lattice dispersion relation (LDR) [28].

We calculate the scattering cross section by simply taking the difference between (3) and (4), i.e., $C_{\text{sca}} = C_{\text{ext}} - C_{\text{ext}}$. Alternatively, a direct and more accurate calculation of scattering cross section can be obtained using the formula defined by Draine [10].

The corresponding extinction, absorption and scattering efficiencies for a sphere with radius a are

$$\begin{aligned} Q_{\text{ext}} &= C_{\text{ext}}/(\pi a^2), \quad Q_{\text{abs}} = C_{\text{abs}}/(\pi a^2), \\ Q_{\text{sca}} &= C_{\text{sca}}/(\pi a^2), \end{aligned} \tag{5}$$

where πa^2 is its cross-sectional area [25].

The standard DDA was designed for modelling free-space light scattering. We use DDA-SI to accommodate the particle sitting on a planar substrate [8, 29]. DDA-SI is a public domain MATLAB toolbox for both free-space and half-space-substrate light-scattering calculations. The interaction between the dipoles and their image counterpart involved decomposing the spherical wave into planar and cylindrical components by means of Sommerfeld integration [30, 31] as did an earlier Fortran implementation of DDA with surface interaction called DDSURF by Schmehl et al. [32].

The relationship [25] between the number of dipoles N, the lattice spacing d and the radius of the target sphere a is

$$Nd^3 = \frac{4}{3}\pi a^3. \tag{6}$$

Strictly speaking, the model is made up of point dipoles, although each dipole occupies a cubic element of volume d^3. The validity criterion for the lattice spacing was defined by Draine and Flatau [25] as

$$d \le \frac{1}{k|n|}, \tag{7}$$

where k is the wave number of the incident field and n is the complex refractive index. However, this assumes that the imaginary component of n is relatively small. For noble metals, the imaginary component of the refractive index is high and increasing towards the IR end of the spectrum. We increase the number of dipoles and thereby decrease d until the solution converges.

2.2 FDTD

FDTD is a popular and an extremely versatile method based on the discretization of Maxwell's curl equations [12, 33]; the numerators and denominators in the derivatives are replaced by corresponding finite spatial elements and temporal steps. The computational domain comprises cuboid volume elements called Yee cells. In some cases, the computational domain is made large enough so that the interaction of interest happens before any wave reaches and reflects off the computational boundary. However, it is beneficial and often essential, in saving computational time and memory usage, to make the computational domain as small as possible by using an absorbing boundary. A popular and effective way is to use the perfectly matched layers (PML) method [34] or subsequent modifications and extensions thereof [35–37].

Unlike the other methods considered here, FDTD is the only time-domain method; thus, discrete time steps are taken to represent time evolution. It also differs from the other methods in that multiple frequencies are simultaneously accounted for during each time step. One notable limitation of FDTD is that if the plane wave is propagating in an oblique direction, the wave front suffers from 'staircasing' due to the spatial discretization. Yee cells are required throughout the whole computational domain, including ambient space; this is computationally expensive especially with 3D FDTD.

For the simulations, we used FDTD Solutions 7.0.1 by Lumerical Solutions [38]. The package allowed for adaptive meshing, i.e., smaller cells where more detail is required and larger cells in other zones save RAM and computational time.

The absorption cross section and efficiency are calculated using the Lumerical built-in functions [38] as follows:

```
# Calculate net power flowing outwards through each active

# monitor:

Px2 = transmission("x2");

Py2 = transmission("y2");

Pz1 =  transmission("z1"); # minus sign due to negative outward-

                                    # pointing surface normal, dS

Pz2 = transmission("z2").

# Use symmetry to get power through each inactive monitor:

Px1 = Px2;

Py1 = Py2.

# Calculate total net power flowing outwards:

P = (Px1 + Px2 + Py1 + Py2 + Pz1 + Pz2)*sourcepower(f).

# Calculate absorption cross-section and efficiency:

P = (Px1 + Px2 + Py1 + Py2 + Pz1 + Pz2)*sourcepower(f).

# Calculate absorption cross-section and efficiency:

Cabs =  P/sourceintensity(f) # minus sign for inward power flow

Qabs = Cabs/(pi*r^2)
```

To ensure causality and numerical stability, the largest time step allowable is limited by the smallest spatial mesh element, whose size is in turn determined by the smallest feature of interest in the simulated geometry. Therefore, using smaller mesh elements in FDTD increases the computational burden both due to the increased number of spatial points and to the smaller time step required for proper convergence. Another issue in FDTD modelling arises when trying to launch a white-light wave at a fixed oblique angle with respect to a planar interface such as a substrate: Since broadband sources inject fields with a constant in-plane wave vector at all frequencies and the magnitude of the total wave vector is proportional to frequency, the actual injection angle will change as a function of frequency [2], thus making a fixed-angle broadband study rather cumbersome due to the necessity to run multiple single-frequency simulations. As this limitation negates the broadband advantage of FDTD for non-normal incidence, we chose not to compare the FDTD method with the other modelling techniques in the cases of oblique illumination.

2.3 FEM

The finite-element method (FEM) [39] involves solving the Helmholtz equation whereby the spatial derivatives at the surface of the scatterer are solved numerically as a boundary value problem. FEM can be used to model the light scattering from arbitrarily shaped, dispersive, inhomogeneous and anisotropic structures for a single frequency at a time. A suitable grid mesh or element (triangular, tetrahedral or hexahedral) is used to represent the surface or structure, with continuity conditions required at adjacent grid cells. The mesh can be denser to represent regions with fine structure.

The steady spatial distribution of $\mathbf{E}$ and $\mathbf{H}$ at the node points is the quantities of interest. The system of linear equations can be solved using Gaussian elimination or the conjugate gradient method. The coefficient matrix for the system of equations represents only the interactions between neighbouring grid mesh cells and thus will be a banded diagonal. The recommended mesh cell size is $\leq \lambda/20$, although $\lambda/5$ has been proven to suffice in some cases.

As with FDTD, the computational region for the FEM is larger than the scatterer. The Helmholtz equation is an elliptic differential equation that is solved as a boundary value problem at the surface at the edge of computational domain (simulating infinity). The most common way to address the radiation condition is with the unimoment method [39]. Other methods of treating the edge of the computational domain include approximate boundary conditions [40] and combining FEM with a surface integral method [41, 42].

For the simulations, we used the FEM implementation of COMSOL Multiphysics 3.5a RF Module [43]. Tetrahedral elements are used to model the structures. The simulation domain is surrounded by the PML absorbing boundary, and additionally, scattering boundary conditions are defined at the outer boundaries [44].

The absorption cross section is calculated using Cabs = 2*Qav_rfw/P0, where Qav_rfw is a COMSOL variable for the resistive heating in half of the particle and P0 = E0^2*0.5*c0_rfw*epsilon0_rfw*n1 is the incident flux. where the variable with the 'rfw' is inherently available in COMSOL [43]. To calculate the scattering cross section, scattered normal flux is integrated over a boundary enclosing the nanoparticle [45], Csca=2*nsc-Poav/P0 where x, y and z-components of the scattered flux,

scPoxav = 0.5 * real(scEy * conj(scHz) − scEz * conj(scHy)),
scPoyav = 0.5 * real(scEz * conj(scHx) − scEx * conj(scHz)),
scPozav = 0.5 * real(scEx * conj(scHy) − scEy * conj(scHx)),

scattered normal flux,

nscPoav = onx * scPoxav + ony * scPoyav + onz * scPozav,

sign factor for the outward normals to interior boundary,

ofact = if(nx * x + ny * y + nz * z > = 0, 1, −1),

and the *x*, *y* and *z*-components of the outward normals to interior boundary,

onx = nx * ofact, ony = ny * ofact, onz = nz * ofact.

2.4 Lorenz–Mie theory

The Lorenz–Mie theory [13, 14, 46] gives the solution to the vector Helmholtz equations for scattering by a homogeneous and isotropic sphere illuminated by an incident plane wave. The scattering cross section can be calculated from the Mie scattering coefficients p_n and q_n:

$$C_{sca} = \frac{2\pi}{k^2} \sum_{n=1}^{\infty} (2n+1)(|p_n|^2 + |q_n|^2), \tag{8}$$

and the extinction cross section is

$$C_{ext} = \frac{2\pi}{k^2} \sum_{n=1}^{\infty} (2n+1)\text{Re}(p_n + q_n). \tag{9}$$

The Mie solution is valid for a sphere of any diameter; large spheres would require more terms in the truncated infinite sum. On the issue of when to apply the Mie solution, as a rule of thumb, any sphere approaching 10 wavelengths in size can be treated with geometric optics, and approaching a tenth of a wavelength, it begins to behave like a dipole, effectively a Rayleigh scatterer; the Mie solution is suitable for a mesoscopic scatterer.

We use the MATLAB Mie scattering implementation by Mätzler [47] to simulate the Au sphere in free space under plane wave illumination.

2.5 NFM-DS

The null-field method with discrete sources (NFM-DS) [15] is a variant of the T-matrix method pioneered by Waterman [16]. In the conventional T-matrix method, the field components comprise spherical vector wave function (SVWF) expansions of the incident, internal and scattered fields. The T-matrix relates the expansion coefficients of the scattered field to those of the incident field. The elements of the T-matrix are computed via surface integration of products of the SVWFs.

In the NFM-DS, the internal field is calculated using the expansion of multiple discrete sources. This allows for the computation of the T-matrix for particles with high aspect ratios. Furthermore, the NFM-DS is not restricted to axis-symmetric scatterers and also allows for particle-surface light scattering. With this method, the exact solution for a particle positioned on or in the vicinity of a planar substrate can be attained [48]. Apart from arbitrary illumination from the upper half-space, surface evanescent wave illumination is also catered for [49].

In order to compute the extinction cross section within the NFM-DS method, we follow the derivation for that of free space by Mishchenko et al. [50]. We integrate the time-averaged pointing vector $\langle \mathbf{S}(\mathbf{r}, t) \rangle$ over the detector area ΔS measuring the internal reflected plane wave

$$W_{\Delta S} \approx (\Delta S - C_{ext}) \cdot I^{LED} + O(r^{-2}),$$
$$C_{ext} = \frac{4\pi}{k_{sub}} \frac{Im(\mathbf{E}^{T+S} \cdot \mathbf{E}^R)}{|\mathbf{E}^R|^2}, \tag{10}$$

where $\mathbf{E}^R$ is the totally internal reflected field, $\mathbf{E}^{T+S}$ is the transmitted field scattered by the particle, k_{sub} is the wave number of the substrate and I^{LED} is the intensity of the incident beam. The transmitted scattered field is expressed as a series of asymptotic functions $(\mathbf{m}_{mn}^{3,T}(\theta, \phi), \mathbf{n}_{mn}^{3,T}(\theta, \phi))$, which are derived from the integral representation of asymptotic radiating SVWFs over plane waves,

using the method of stationary phase for integral evaluation by Doicu et al. [49].

Our approach enables a very accurate computation of the extinction cross section within the T-matrix method for particles of arbitrary shape, illuminated by an evanescent wave. Similar formulae for clustered spherical particles and non-evanescent illumination were obtained by Mackowski [51]. In spite of the other widely used approximation, we do not neglect the particle–surface interaction and the derivation of the incident field over the particle surface [52].

3 Test configurations and results

The calculations were performed on different computers with different operating systems, and thus, the meaningful time comparison data cannot be presented here. However, the priority was to cross-validate DDA-SI against other modelling methods.

3.1 Plane wave illumination

The first test scenario (Fig. 1a) involves the Au nanosphere illuminated by a plane wave where Q_{ext}, Q_{abs} and Q_{sca} results of DDA, FEM and FDTD calculations are compared against those of the Mie solution (Fig. 4). The number of dipoles used for the DDA simulations was $N = 552$ and $N = 4,224$ for the sphere diameters of 50 nm and 200 nm, respectively. Overall DDA appears most inaccurate benchmarked against the Mie solution, and more so for the smaller 50-nm particle. This is not due to the lattice spacing not being small enough because even with greater

Fig. 4 Q_{ext}, Q_{abs} and Q_{sca} efficiency spectra of the 50-nm (*left column*) and 200-nm (*right column*) Au nanosphere in free space, illuminated by a plane wave
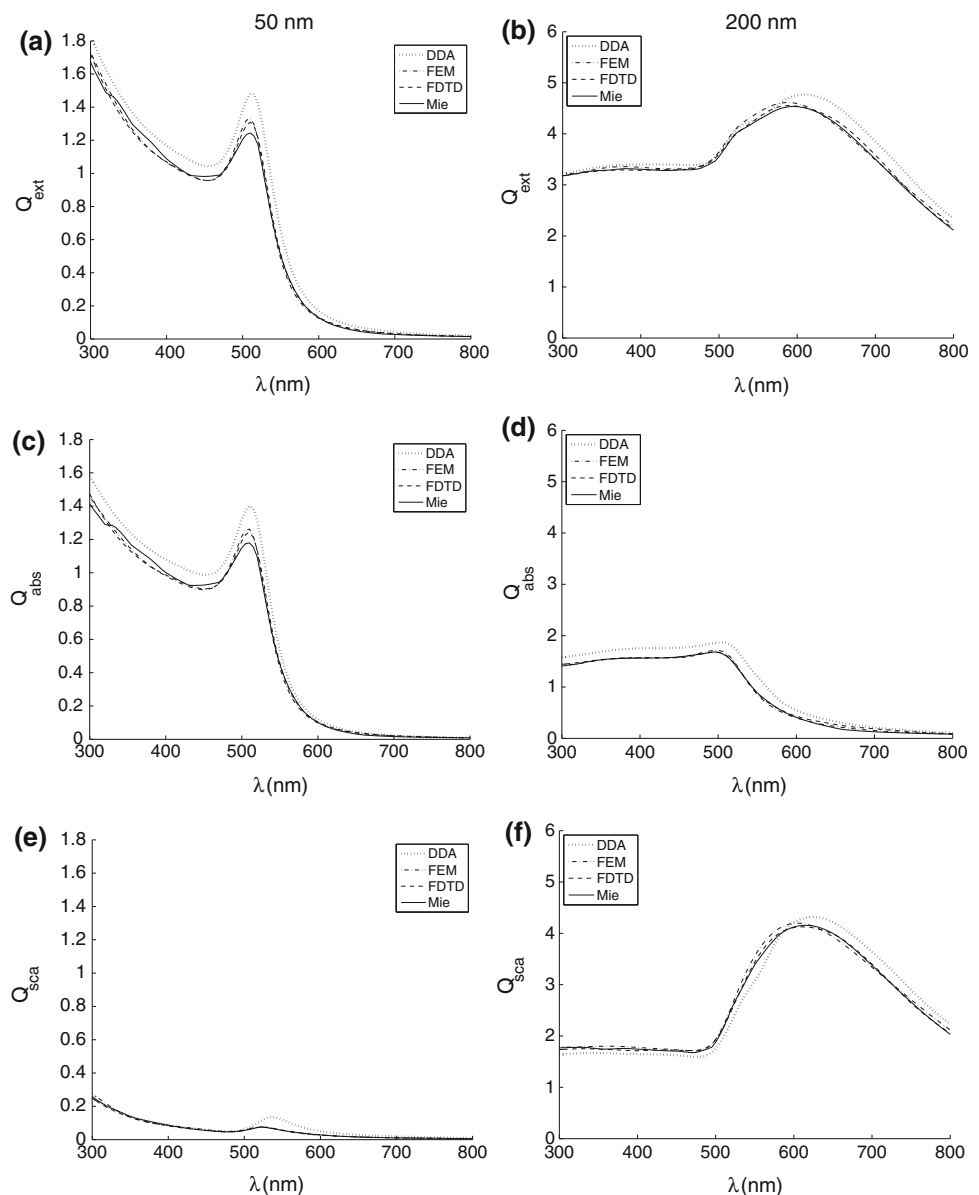
Fig. 5 Q_{ext}, Q_{abs} and Q_{sca} efficiency spectra of the 50-nm (*left column*) and 200-nm (*right column*) Au nanosphere sitting on a BK7 glass planar substrate, illuminated by a plane wave propagating in normal to the surface
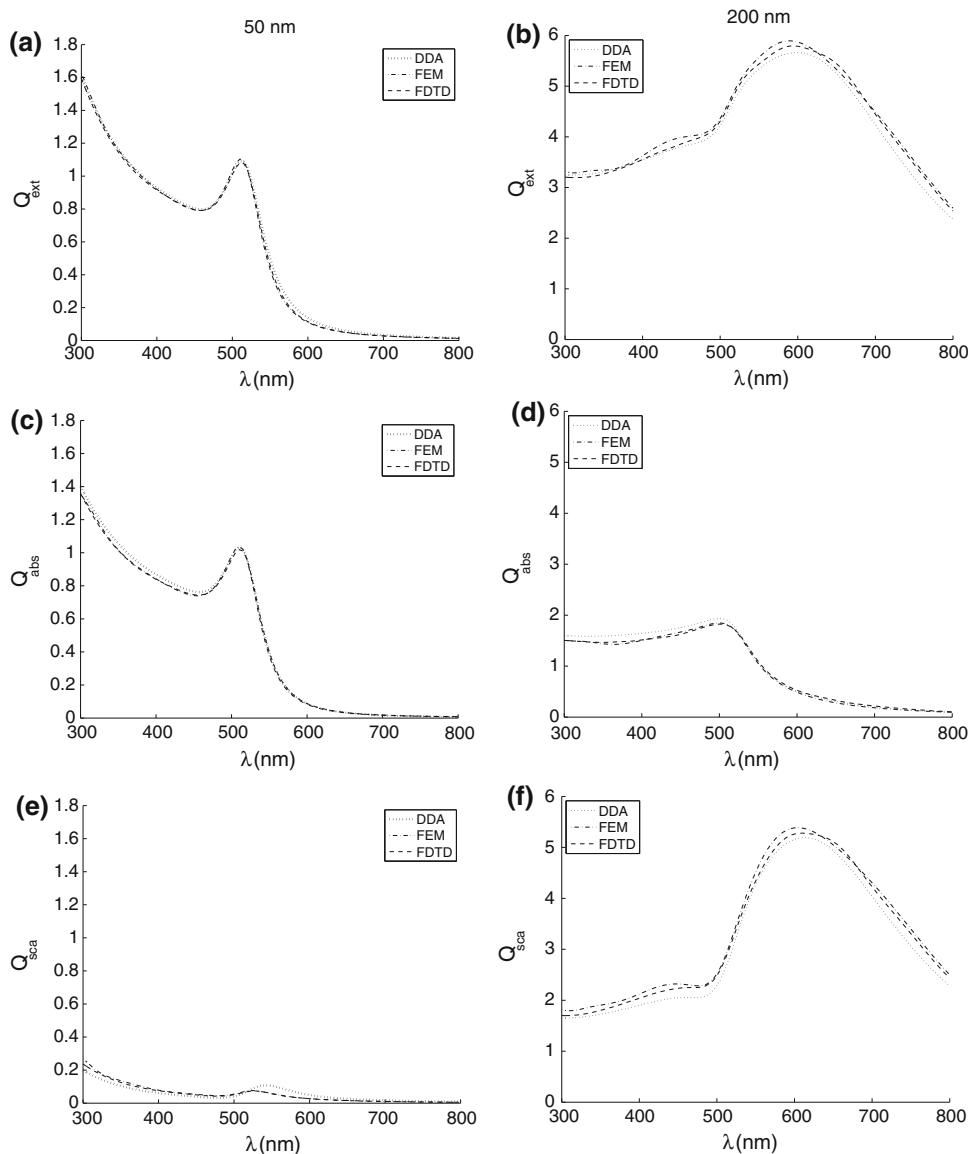
number of dipoles the Q_{ext} and Q_{abs} results converge as if they are offset above the results from the other models, i.e., as if the approximate sphere was slightly larger than the target sphere.

Next, the particle is placed on a planar BK7 substrate whilst the incident beam is the direction normal to the surface (Fig. 1b). Here, the Q_{abs} and Q_{sca} results (Fig. 5) for DDA are more consistent with FEM and FDTD when compared to the free-space scenario. Here, the numbers of dipoles used were $N = 552$ and $N = 4{,}224$ for the sphere diameters of 50 nm and 200 nm, respectively, although it was found that, in the presence of the substrate, convergence is achieved with a smaller number of dipoles.

In comparing the results between the different-sized spheres, for both the free-space and substrate scenarios, it is evident that for the larger particle, scattering becomes more dominant than absorption.

3.2 Evanescent wave illumination

When a plane wave undergoes total internal reflection as shown in Fig. (2), there will still be a complex wave vector and polarization vector beyond the media interface [53], which result in an evanescent wave on the surface of the substrate. Here, we set the incident angle at 70° and the ambient medium was water, with the dispersion-free refractive index of $n = 1.33$. The simulated evanescent wave and nanoparticle for the FEM model were based on previous work by Huda et al. [44].

In the case of the TE incident wave, the resultant evanescent field has only the component parallel to the planar interface, whereas for the TM incident wave, both the parallel and perpendicular components exist. Thus, there will be more evanescent wave coupling in the TM case on which we base our calculations.

Fig. 6 The **a** absorption and **b** extinction efficiency spectra of a 50-nm Au nanosphere under evanescent wave illumination (TM), calculated using DDA-SI and FEM, and in **b** also compared against the NFM-DS
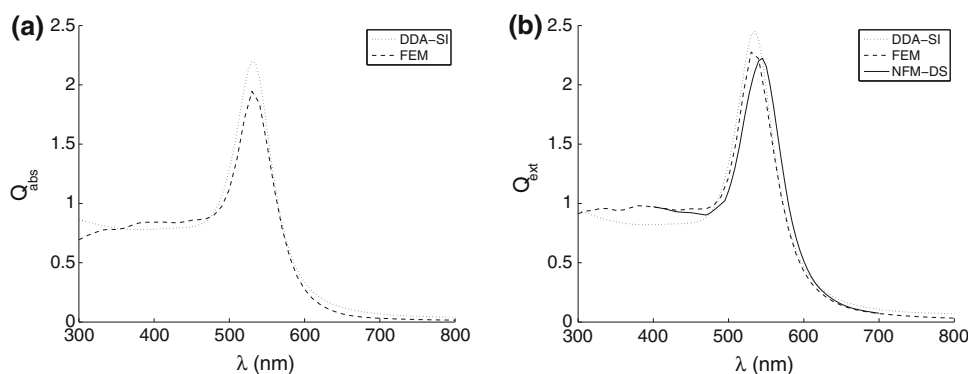

Figure 6 shows the absorption and extinction efficiency spectra of a 50-nm Au sphere on a BK7 glass substrate undergoing TM evanescent field illumination where comparisons are made between DDA-SI and FEM. The extinction efficiency spectrum is also verified against that of the NFM-DS analytical solution. The number of dipoles used for the DDA-SI simulations was $N = 912$.

4 Discussion

For DDA, we modelled approximate spheres without any volume correction suggested by Draine [10] and Yurkin et al. [54]; this does not result in significant errors in the cases where the refractive index contrast between the scatterer and the ambient medium is low, e.g., for water spheres [8]. However, in our DDA results for the Au sphere in free space (Fig. 4), the Q_{ext} and Q_{abs} spectra for DDA appear as if the particle radius is about 3% larger than it should be. This is due to the high imaginary component of the refractive index of Au (Fig. 3a) that not only requires higher number of dipoles for the model but exacerbates errors due to the lack of volume correction. Yurkin et al. [55] specifically address the accuracy of DDA when simulating Au nanoparticles. Improvements to the accuracy may also be achieved by using the filtered coupled dipoles (FCD) [56] method for calculating the dipole polarizability.

Generally, as can be seen in Eq. (7), smaller lattice spacings are required in the shorter wavelength regime. Au and other metals such as Ag, Al and Cr have imaginary components in their refractive indices that increase with the wavelength to very high levels. This means that modelling these metals, in comparison with other materials, requires a relatively large number of dipoles per unit volume throughout the whole spectrum ranging from UV to IR.

In the case of the plane wave illumination for the Au sphere on a BK7 glass substrate, the DDA-SI results were in good agreement with those of FEM and FDTD (Fig. 5), even without volume correction. We speculate that this is due to the lower half-space medium being glass having the

effect of reducing the overall refractive index contrast of Au. We also found that although we used the same corresponding numbers of dipoles as those of the free-space scenario, our preliminary results with fewer of dipoles were quite satisfactory. This suggests that the substrate helps with convergence, due to the lower refractive index contrast.

Under the simulated evanescent TM illumination, the Q_{abs} and Q_{ext} spectra (Fig. 6) from the DDA-SI and FEM calculations are reasonably consistent. The additional comparison with the Q_{ext} spectrum calculated using the NFM-DS further validated the results.

The DDA-SI MATLAB toolbox [8] can be downloaded from https://code.google.com/p/dda-si/. In addition to the evanescent wave example we presented here, it can be used with arbitrary illumination ranging from plane waves, dipole sources, focussed laser beams (e.g., Gaussian, Laguerre-Gauss and Bessel), field emanating from a moving charge [57] or any valid form of electric field distribution, propagating in any direction; reflection and transmission at the planar interface will have to be addressed. Multiple scatterers with arbitrary shapes and any combination of complex refractive indices may be used. The planar substrate may also have an arbitrary complex refractive index; the interaction with the planar surface involves contour integration of the complex wave vectors outlined in detail in [26, 58].

The field from a dipolar source can be obtained from the Green's tensor (2) where it is evident that the far-field term is dependent on $1/r$ whereas the near-field term is evanescent, i.e., diminishes rapidly with distance, proportional to $1/r^3$. Thus, in the scenario involving a dipolar source in contact with a nanoparticle or any simulation involving near-field coupling for that matter, the field gradients can be very high. To avoid significant errors in DDA or DDA-SI, it is required that lattice spacings be small enough to effectively capture the high-field gradients with respect to displacement. The equivalent approach for FDTD and FEM would use smaller grid spacings and mesh sizes, respectively.

5 Conclusion

We benchmarked the DDA-SI MATLAB toolbox against the FEM, FDTD, Mie solution and NFM-DS for the accuracy when modelling surface plasmon resonance. Without volume correction, the free-space DDA calculations presented errors that appear as an offset in the Q_{abs} and Q_{ext} spectra, as if representing a marginally larger particle. However, this error is eliminated in the DDA-SI implementation where the particle sits on a substrate; we propose that although the substrate exists only in the lower half-space, it causes a reduction in the overall contrast of the refractive index between the scatterer with its environment.

Overall, the vastly different modelling methods produce consistent results in cross-validating the plasmonic response of the test 50 and 200-nm Au spheres, illuminated by a plane wave in free space and on a substrate and illuminated by an evanescent wave. All the methods above are derived from Maxwell's equations. In spite of their naivety in having no knowledge and no explicit implementation of the collective oscillation of valence electrons resonating with the incident field, the surface plasmon resonance phenomenon is reproduced.

References

1. T. Nagao, G. Han, C. Hoang, J.S. Wi, A. Pucci, D. Weber, F. Neubrech, V.M. Silkin, D. Enders, O. Saito, M. Rana, Sci. Tech. Adv. Mater. **11**, 054506 (2010)
2. B. Schaffer, U. Hohenester, A. Trugler, F. Hofer, Phys. Rev. B **79**, 041401 (2009)
3. D.G. Georganopoulou, L. Chang, J.M. Nam, C.S. Thaxton, E.J. Mufson, W.L. Klein, C.A. Mirkin, Proc. Natl. Acad. Sci. USA. **102**, 2273–2276 (2005)
4. J.C.Y. Kah, K.W. Kho, C.G.L. Lee, C.J.R. Sheppard, Z.X. Shen, K.C. Soo, M.C. Olivo, Int. J. Nanomed. **2**, 785–798 (2007)
5. H.M. Hiep, T. Endo, K. Kerman, M. Chikae, D.K. Kim, S. Yamamura, Y. Takamura, E. Tamiya, Sci. Tech. Adv. Mater. **8**, 331–338 (2007)
6. R. Esparza, G. Rosas, E. Valenzuela, S.A. Gamboa, U. Pal, R. Perez, Materia-Rio de Janeiro **13**, 579–586 (2008)
7. M.P. Pileni, J. Phys. **23**, 503102 (2011)
8. V.L.Y. Loke, M.P. Mengüç, T.A. Nieminen, JQSRT **112**, 1711–1725 (2011)
9. E. Purcell, C. Pennypacker, Astrophys. J. **186**, 705–714 (1973)
10. B. Draine, Astrophys. J. **333**, 848–872 (1988)
11. S. Ahmed, Electron. Lett. **4**, 387–389 (1968)
12. K.S. Yee, IEEE Trans. Antenn. Propag. **14**, 302–307 (1966)
13. L. Lorenz, Videnskabernes Selskabs Skrifter **6**, 2–62 (1890)
14. G. Mie, Ann. Phys. **25**, 377–445 (1908)
15. T. Wriedt, JQSRT **106**, 535–545 (2007)
16. P.C. Waterman, Proc. IEEE **53**, 805–812 (1965)
17. T. Wriedt, JQSRT **110**, 833–843 (2009)
18. J. Parsons, C.P. Burrows, J.R. Sambles, W.L. Barnes, J. Mod. Opt. **57**, 356–365 (2010)
19. X.H. Huang, P.K. Jain, I.H. El-Sayed, M.A. El-Sayed, Lasers Med. Sci.**23**, 217–228 (2008)
20. K.M.M. Aung, Y.N. Tan, K.V. Desai, X.D. Su, Aust. J. Chem. **64**, 1286–1292 (2011)
21. M. Quinten, *Optical Properties of Nanoparticle Systems: Mie and Beyond*. (Wiley, New York, 2011)
22. A. Vial, T. Laroche, Appl. Phys. B **93**, 139–143 (2008)
23. W. Sellmeier, Ann. Phys. Chem. **219**, 272–282 (1871)
24. R. Luebbers, F.P. Hunsberger, K.S. Kunz, R.B. Standler, M. Schneider, IEEE Trans. Electromagn. Compat. **32**, 222–227 (1990)
25. B.T. Draine, P.J. Flatau, J. Opt. Soc. Am. A **11**, 1491–1499 (1994)
26. V.L.Y. Loke, M.P. Mengüç, in Proceedings of ELS XII Helsinki 134–137 (2010)
27. Y. Saad, M.H. Schultz, SIAM J. Sci. Stat. Comput. **7**, 856–869 (1986)
28. B.T. Draine, J. Goodman, Astrophys. J. **405**, 685–697 (1993)
29. V.L.Y. Loke, M.P. Mengüç, J. Opt. Soc. Am. A **27**, 2293–2303 (2010)
30. A. Sommerfeld, Ann. Physik **28**, 665–736 (1909)
31. W.C. Chew, *Waves, Fields in Inhomogeneous Media*. (Van Nostrand Reinhold, New York, 1990)
32. R. Schmehl, B.M. Nebeker, E.D. Hirleman, J. Opt. Soc. Am. A **14**, 3026–3036 (1997)
33. A. Taflove, S.C. Hagness, *Computational Electrodynamics: The Finite-Difference Time-Domain Method*, 3rd edn. (Artech House, Boston, 2005)
34. J.P. Berenger, J. Comput. Phys. **114**, 185–200 (1994)
35. Z.S. Sacks, D.M. Kingsland, R. Lee, J.F. Lee, IEEE Trans. Antenn. Propag. **43**, 1460–1463 (1995)
36. S. Gedney, IEEE Trans. Antennas Propagat **AP-44**, 1630–1639 (1996)
37. J.A. Roden, S.D. Gedney, Microw. Opt. Tech. Lett. **27**, 334–339 (2000)
38. Lumerical FDTD Solutions Package Reference Guide for FDTD Solutions v7.0.1 ed (2010)
39. M.A. Morgan, K.K. Mei, IEEE Trans. Antenn. Propag. **27**, 202–214 (1979)
40. R. Mittra, O. Ramahi, Finite element and finite difference methods in *Electromagnetic Scattering*, vol. II, ed. by M. Morgan (Elsevier, New York, 1990)
41. J.L. Volakis, A. Chatterjee, L.C. Kempel, *Finite Element Method for Electromagnetics*. (IEEE Press, New York, 1998)
42. X.Q. Sheng, J.M. Jin, J.M. Song, C.C. Lu, W.C. Chew, IEEE T. Antenn. Propag. **46**, 303–311 (1998)
43. COMSOL Multiphysics RF Module Reference Guide v3.5a ed (2008)
44. G.M. Huda, E.U. Donev, M.P. Mengüç, J.T. Hastings, Opt. Express **19**, 12679–12687 (2011)
45. COMSOL Mie scattering off plasmonic nanoparticle and radar cross-section computations (2008) http://www.comsol.com/showroom/gallery/3459/
46. P. Debye, Ann. Phys. **30**, 57–136 (1909)
47. C. Mätzler, MATLAB functions for Mie scattering and absorption v2 Tech. Rep. Research Report No. 2002-11 University of Bern (2002)
48. A. Doicu, Y.A. Eremin, T. Wriedt, Opt. Commun. **159**, 266–277 (1999)
49. A. Doicu, Y. Eremin, T. Wriedt, Comput. Phys. Commun. **134**, 1–10 (2001)
50. M.I. Mishchenko, L.D. Travis, A.A. Lacis, *Multiple Scattering of Light by Particles: Radiative Transfer and Coherent Backscattering*. (Cambridge University Press, Cambridge, 2006)

51. D.W. Mackowski, JQSRT 109 770–788 ISSN 0022-4073 (2008) http://www.sciencedirect.com/science/article/pii/S0022407307002282

52. M. Quinten, A. Pack, R. Wannemacher, Appl. Phys. B **68**, 87–92 (1999)

53. M. Born, E. Wolf, *Principles of Optics*, 7th edn. (Cambridge University Press, Cambridge, 1999)

54. M.A. Yurkin, A.G. Hoekstra, JQSRT **112**, 2234–2247 (2011)

55. M.A. Yurkin, de D. Kanter, A.G. Hoekstra, J. Nanophoton. **4**, 041585 (2010)

56. M.A. Yurkin, M. Min, A.G. Hoekstra, Phys. Rev. E **82**, 036703–12 (2010)

57. N. Geuquet, L. Henrard, Ultramicroscopy **110**, 1075–1080 (2010)

58. R.J. Lytle, D.L. Lager, Numerical evaluation of Sommerfeld integrals. Technical report (1974). UCRL-51688 Lawrence Livermore Laboratory Livermore, California